

**Some supplementary files may need to be viewed online via your Referee Centre at <http://mc.manuscriptcentral.com/nar>.**

**Ensemble Simulations: Folding, Unfolding, and Misfolding of  
a High-Efficiency Frameshifting RNA Pseudoknot**

Journal:	<i>Nucleic Acids Research</i>
Manuscript ID	NAR-02257-R-2016.R1
Manuscript Type:	1 Standard Manuscript
Key Words:	conformational plasticity, self-assembly, luteovirus, PLRV, distributed computing

SCHOLARONE™  
Manuscripts

1  
2  
3  
4  
5  
6  
7  
8  
9  
10  
11  
12  
13  
14  
15  
16  
17  
18  
19  
20  
21  
22  
23  
24  
25  
26  
27  
28  
29  
30  
31  
32  
33  
34  
35  
36  
37  
38  
39  
40  
41  
42  
43  
44  
45  
46  
47  
48  
49  
50  
51  
52  
53  
54  
55  
56  
57  
58  
59  
60

**Ensemble Simulations: Folding, Unfolding, and Misfolding of a  
High-Efficiency Frameshifting RNA Pseudoknot**

Khai K. Q. Nguyen<sup>†,1,2</sup>, Yessica K. Gomez<sup>†,1,3</sup>, Mona Bakhom<sup>1</sup>, Amethyst Radcliffe<sup>3</sup>,  
Phuc La<sup>1</sup>, Dakota Rochelle<sup>1</sup>, Ji Won Lee<sup>1</sup>, and Eric J. Sorin<sup>1,\*</sup>

Departments of <sup>1</sup>Chemistry & Biochemistry,  
<sup>2</sup>Computer Engineering & Computer Science, and  
<sup>3</sup>Physics & Astronomy  
California State University Long Beach,  
Long Beach, California 90840, United States

<sup>†</sup>The authors wish it to be known that, in their opinion, the first two authors should be regarded as joint First Authors

Running Title: RNA Pseudoknot Folding & Misfolding Simulations

Keywords: distributed computing, self-assembly, luteovirus, PLRV, conformational plasticity

\*Corresponding Author  
Eric J. Sorin, Associate Professor  
Department of Chemistry & Biochemistry  
California State University Long Beach  
1250 Bellflower Blvd.  
Long Beach, California 90840-9401, USA  
Phone: 562-985-7537  
URL: <http://chemistry.csulb.edu/esorin/>  
Email: [eric.sorin@csulb.edu](mailto:eric.sorin@csulb.edu)

## ABSTRACT

Massive all-atom molecular dynamics simulations were conducted across a distributed computing network to study the folding, unfolding, misfolding, and conformational plasticity of the high-efficiency frameshifting double mutant of the 26 nt potato leaf roll virus RNA pseudoknot. Our robust sampling, which included over 40 starting structures spanning the spectrum from the extended unfolded state to the native fold, yielded nearly 120  $\mu$ s of cumulative sampling time. Conformational microstate transitions on the 1.0 ns to 10.0  $\mu$ s timescales were observed, with post-equilibration sampling providing detailed representations of the conformational free energy landscape and the complex folding mechanism inherent to the pseudoknot motif. Herein, we identify and characterize two alternative native structures, three intermediate states, and numerous misfolded states, the latter of which have not previously been characterized via atomistic simulation techniques. While in line with previous thermodynamics-based models of a general RNA folding mechanism, we find that stem-strand-sequence-separation may serve as an alternative predictor of the order of stem formation during pseudoknot folding. Our results contradict a model of frameshifting based on structural rigidity and resistance to mechanical unfolding, and instead strongly support more recent studies in which conformational plasticity is identified as a determining factor in frameshifting efficiency.

## INTRODUCTION

The RNA pseudoknot motif is a well-characterized supersecondary structure that contains two (or more) base-paired stem regions in which a strand of one of these stems is intercalated within the two strands of another stem (Figure 1a). Discovery of RNA pseudoknots began in the late 1970's with the observation of tRNA mimicry by the 3' terminal pseudoknot of Turnip Yellow Mosaic Virus (TYMV) (1), which shares neither primary nor secondary structure with tRNA<sup>Val</sup>, yet achieves recognition by tRNA<sup>Val</sup>-specific enzymes (2,3). Mimicry-capable RNAs, such as TYMV, showcase the potential dominance of three-dimensional topology, rather than primary or secondary structure, in determining the biological activity of RNAs (4).

In recent years, pseudoknots have been observed to play functional roles in structural organization, ribosomal association, and translation via unfolding and refolding (5), and particular attention has been given to the participation of pseudoknots in -1 programmed

1  
2  
3 ribosomal frameshifting (PRF), the register shifting of the mRNA translational reading frame  
4 that alters codon recognition, as observed in *Luteovirus*, HIV-1, and coronaviruses (6,7).  
5 Frameshifting, including -1 PRF, is now understood to be enabled through the presence of two  
6 fundamental motifs in viral mRNA during translation: an upstream heptanucleotide slippery  
7 sequence, where the pausing of the ribosome and displacement of the reading frame occurs, and  
8 a downstream stimulatory element (the pseudoknot). Frameshifting ability thus serves as an  
9 important recoding strategy that allows a virus to maximize the number of polypeptides encoded  
10 by a relatively small genome (8).  
11  
12

13  
14 While it was previously proposed that rigid, highly stable pseudoknots would resist  
15 unfolding and thereby lead to frameshifting (9), more recent studies have suggested that  
16 frameshifting efficiency instead depends on the overall conformational plasticity of the  
17 pseudoknot (8), which is defined by the diversity of unfolded, partially folded, and alternative  
18 states within the conformational equilibrium, in tandem with the ability of native structures to  
19 readily undergo transitions to these non-native states.  
20  
21

22  
23 The dynamic nature of RNA structure, and the relation of such structural dynamics to  
24 function, emphasizes the notion that the lowest energy structure is not always representative of  
25 the functional conformation (10), highlighting a key problem with analyses based upon a single  
26 energy-minimized structure, and thereby presenting a challenge in better understanding RNA  
27 structure-function relationships. Further complicating this matter, the free energy landscape  
28 often features an ensemble of partially folded and misfolded states (11,12), some of which may  
29 have functional utility enabled through alternative geometries. For example, the tRNA-mimic  
30 pseudoknot of TYMV can also modulate ribosome and replicase activity of genomic RNA in  
31 TYMV (13).  
32  
33

34  
35 This study seeks to characterize the free energy surface and conformational dynamics of  
36 the potato leaf roll virus (PLRV) RNA pseudoknot via massive all-atom molecular dynamics  
37 (MD) simulations, which provide structural information about native, non-native, and misfolded  
38 states along the folding pathway. PLRV is classified within the *Luteoviridae* family and shares  
39 the *Polerovirus* genus with beet western yellow virus (BWYV), a widely known and highly  
40 studied RNA pseudoknot. The PLRV used herein (PDB 2A43, shown in Figure 1b) is an X-ray  
41 crystallographic structure which possesses C17U/A18C mutations that greatly enhance its  
42 frameshifting efficiency (9). This PLRV exhibits considerable structural and spatial homology  
43  
44  
45  
46  
47  
48  
49  
50  
51  
52  
53  
54  
55  
56  
57  
58  
59  
60

with BWYV (14), thus making it a strong candidate for studies in RNA folding and dynamics, and pseudoknot structure-activity analysis, such as understanding the role of conformational dynamics in -1 PRF.

## METHODS

The PLRV pseudoknot was studied via all-atom molecular dynamics simulations using the AMBER potential (15) ported to the GROMACS 3.3 molecular dynamics suite (16). Charge neutrality was obtained through inclusion of 25 Na<sup>+</sup> ions (17) placed randomly around the solute with a minimum RNA-ion separation of 5.0 Å, resulting in an ionic concentration of approximately 100 mM. Steepest-descent energy minimization was followed by solvation in a periodic 75 Å cubic box with approximately 13,500 TIP3P water molecules (18) to capture both the bulk and molecular properties of the ionic aqueous solvent, which was then annealed with the RNA held fixed for 1.0 ns prior to the collection of production simulations. All simulations were run in the NPT ensemble (19) at 1 atm and 300 K using a 2.0 fs timestep with bonds constrained using the LINCS algorithm (20) and conformations stored every 100 ps. No artificial biasing potentials or restraints were employed.

The resulting thermodynamically-stable system served as the starting point for 20 thermal unfolding simulations, which generated thousands of conformations spanning the complete (un)folding pathway. Although high-temperature unfolding simulations are not expected to generate misfolded structures or alternative folds, this method provides the energy necessary to overcome, and thus sample both sides of, large conformational free energy barriers, making it a simple and powerful tool with which to sample conformations along the (un)folding pathway. Our previously reported K-means clustering algorithm (21) was then applied to the structures resulting from these thermal unfolding simulations, each of which was represented by a four dimensional vector defined by the pseudoknot radius of gyration ( $R_g$ ), the all-atom root-mean-squared deviation (RMSD) from the native starting structure, and the number of native and non-native base-pairing interactions, as determined by the 3DNA analysis tool (22). This clustering resulted in 41 distinct conformational clusters ranging from fully unfolded, with an RMSD of 30.1 Å and a radius of gyration of 31.7 Å, to fully folded (RMSD of 0.0 Å and  $R_g$  of 11.9 Å).

The average structure within each of these 41 clusters was then identified and served as the starting point for 200 all-atom, explicit-solvent MD simulations at 300 K and 1 atm, thereby

totalling 8,200 independent simulations collected on the Folding@Home distributed computing network (<http://folding.stanford.edu>) (23). As illustrated in Figure 2, the initial phase of our simulations consisted of ensemble-level annealing of each of the 41 starting structures on the 300 K free energy surface, followed by random transitions between energetic minima. While our use of numerous and conformationally-diverse starting structures cannot guarantee that all regions of the conformational space have been sampled, the approach taken herein was designed to optimize the sampling of conformational states, and transitions between these states, and our cumulative sampling time of nearly 120  $\mu$ s represents a significant move forward in making the examination of that space at the all-atom level as thorough as possible, yielding a richly detailed description of pseudoknot structure and dynamics, as described below.

K-means clustering of the resulting data set (nearly 1.2 million structures) following the protocol described above yielded 27 conformational microstates, with no significant overlap between neighboring clusters, and transitions between neighboring clusters occurring on the 1.0 ns to 10.0  $\mu$ s timescales. The population of each conformational microstate as a function of time within our simulated ensemble was monitored, with approximate conformational equilibrium reached at 6.0 ns (Figure 3). We emphasize that the approximate equilibrium suggested in Figure 3 represents a steady-state within our simulated ensemble on the 100  $\mu$ s timescale. Transitions involving larger free energy barriers and longer timescales may, therefore, have gone unobserved within our ensemble simulations. To confirm steady-state behaviour, the transition probability and rate matrices, representing the moves from each microstate  $i$  to each microstate  $j$  after the equilibration period, were evaluated and demonstrated both time-independence and detailed balance. Post-equilibration sampling, which included over 50  $\mu$ s of simulation time, was therefore used to evaluate the thermodynamics, kinetics, and folding mechanism of the pseudoknot motif.

To quantitatively assess the native structural content of each of our approximately 1.2 million simulated conformations, native contacts (NC) were defined as atomic pairs separated by 3 or more residues that were within 5.0 Å of one another at least 25% of the time in our simulated native state ensemble, thereby accounting for native state structural flexibility (24). Simulations were considered as part of the native state ensemble if they maintained an all-atom RMSD below 5.0 Å, thereby yielding a total native state simulation time of 8.44  $\mu$ s across 1,175 simulations. Native contacts for each conformation were then identified for the full pseudoknot

structure and for each substructure within the pseudoknot motif. The resulting native contact counts were then normalized using the mean number of native contacts observed in native state simulations; for tertiary (T) native contacts and those in Loop 2 (L2), both of which displayed multi-modal distributions, normalization was done using the maximum in the highest-valued peak in the NC distribution. Contacts between atomic pairs not observed in the simulated native state ensemble were classified as non-native contacts (NNC), an atomic-level analog of the recently-published NNC definition of Mouro *et al.* (25), and normalized using the largest quantity of non-native contacts observed. We emphasize that this latter normalization of non-native contacts may underscore the overall degree of non-native character, and thus the degree of misfolding, present within a given structure.

## RESULTS & DISCUSSION

### *Pseudoknot Structural States*

The conformational free energy surfaces shown in Figure 4 are projected onto four metrics: the all-atom RMSD, the radius of gyration, and the normalized quantities of both native and non-native contacts, as defined above. These free energy landscapes were visualized, using only post-equilibration data from our simulated ensemble, by defining the free energy as  $F = -RT \ln Pr$  at 300 K, where  $Pr$  is the normalized probability of finding structures at a given location on the energy landscape. Partitioning of the four-dimensional space depicted in Figure 4 led to the identification of 11 conformational macrostates. In describing these macrostates below, and as labeled in Figure 4c, capital F, I, M, and U labels were used to denote folded, intermediate, misfolded, and unfolded states, respectively, with numeric subscripts ranging from most native (lower subscript values) to least native (higher subscript values). **The overall native and non-native character of these 11 macrostates, alongside the mean native character of substructures within the pseudoknot motif, are provided in Table 1.**

*Native states.* The upper left corners of Figures 4c and 4d, which represent structures with low RMSD, high NC, and zero NNC, demonstrate the presence of two alternative folded states (NC > 90%, RMSD < 5 Å). The state denoted as F<sub>1</sub> averages only ~2.0 Å RMSD from the crystal structure and contains a well-structured Loop 2 region. In contrast, the state labeled F<sub>2</sub>, with an average RMSD of ~3.7 Å RMSD from the crystal structure, contains a significantly less-

structured Loop 2 region and increased native tertiary contacts (Table 1). As tertiary structure in the PLRV pseudoknot is formed predominantly through interactions of Loop 2 bases with the minor groove of Stem 1 (S1) to form a “triple helix” structure (26), which has been observed in other pseudoknots (27), our observation of alternating Loop 2 and tertiary contacts suggests a twisting mode in which either Loop 2 or tertiary contacts may be optimally sampled to increase the overall stability of the pseudoknot fold.

To probe this possibility, and to assess the overall flexibility of each residue in the PLRV pseudoknot, the all-atom root-mean-squared fluctuations (RMSF) were plotted and the mean structures representing these two alternative states were compared. As shown in Figure 5a, which includes only data from our reported 8.44  $\mu$ s of native state simulations, nearly all Loop 2 residues from A19 to A25 (inclusive) exhibit significant RMSF, with fluctuations of approximately 5 – 8 Å. Only the U12 “bridge” residue between the two stem regions shows more flexibility than Loop 2 residues. In addition, Loop 1 (L1) residues (C7 and A8) show moderate flexibility (RMSF of 4 – 5 Å), which is clearly limited by the size of the loop and the stability of G•C base-pairs on either side of this loop region.

The high flexibility of Loop 2 in the PLRV pseudoknot is not surprising given its sequence size of 9 nt: Reiling *et al.* recently reported a direct correlation between loop size and flexibility, and characterized the optimization of base-pair stacking interactions that can result from such flexibility (28), which contributes to the inherent entropy of Loop 2 while also providing alternative structural interactions within the pseudoknot. A comparison of the mean structures of states F<sub>1</sub> and F<sub>2</sub> is shown in Figure 5b, with Figure 5c showing these same structures rotated 90° about the vertical axis. The primary differences between these two states is the looping out of residues A21 and C22, and a slight unwinding of both helical stem regions to facilitate increased tertiary contacts in state F<sub>2</sub>. These include interactions between the Loop 2 backbone and Stem 1, the A23 residue and the Stem 1 backbone, and improved stacking and hydrophobic packing interactions within the two helix stem regions.

Unlike the majority of Loop 2 residues, A20 and A24 show relatively low mobility in Figure 5a, which is due to the participation of these two residues in base-triplets, as shown in Figure 5d. Hydrogen bonding and van der Waals contact between the bases of A20 and A24 with the G3•C16 and G6•C13 base-pairs, respectively, effectively anchor both Stem 1 and these



Loop 2 residues in place in both the  $F_1$  and  $F_2$  native states, while leaving U12, Loop 1, and most of Loop 2 flexible enough to allow rapid transitions between  $F_1$  and  $F_2$ .

*Intermediate states.* Below the states labeled  $F_1$  and  $F_2$  in Figure 4c, **three intermediate states (labeled  $I_1$  through  $I_3$ ) were identified by their significant quantities of native structure and low degrees of non-native interactions.** Our observation of multiple intermediates in pseudoknot folding agrees with numerous previous observations and predictions including the simple model of Ansari and coworkers based on laser T-jump experiments (29) and the folding pathways predicted from coarse-grained simulations by Thirumalai and coworkers (30). While both  $I_1$  and  $I_2$  have undergone collapse to a near-native mean gyration radius of just over 12 Å in our simulated PLRV ensemble, the  $I_3$  state is somewhat less compact with an average gyration radius of 15.5 Å, and significant differences are apparent among these three states.

**The least native of these three intermediates,  $I_3$ , has a mean RMSD of approximately 15 Å and contains limited native structure with 33.7(±3.3)% of native contacts present, which derive solely from the 84.7(±11.4)% of Stem 1 formation, on average, with no other appreciable native structure observed (Table 1). The small degree of non-native interaction observed in  $I_3$ , 12.4(±6.0)%, is largely due to interactions between residues 19 – 23 (Loop 2 residues) that fold back upon Stem 1 to stabilize that stem and to interact with the 5' terminus.**

In contrast, the  $I_2$  intermediate (mean RMSD of ~8 Å) contains 50.5(±6.2)% of global native contacts and the more native-like  $I_1$  intermediate (mean RMSD of ~5 Å) contains an average of 67.8(±3.9)% of global native contacts, demonstrating a significant decrease in RMSD and an increase in native character of nearly 20% as folding progresses from each intermediate to its more native neighboring state. While  $I_1$  contains a fully formed Stem 1 helix and ~22% of Stem 2 contacts,  $I_2$  has an average Stem 1 native content of only 73.9(±18.7)% (statistically equivalent to Stem 1 content in the  $I_3$  intermediate) and an average Stem 2 native content of 12.2(±28.5)%, indicating that S2 nucleation occurs as intermediate  $I_2$  is reached. Whereas the Loop 2 region shows an average of 20 – 25% of native structure formed in both the  $I_1$  and  $I_2$  intermediate states, the Loop 1 region, which consists of only 2 nucleotides and a relatively small number of native contacts, is fully formed in the observed  $I_1$  intermediate but remains unstructured in the less-native  $I_2$  and  $I_3$  states.

As with  $I_3$ , the  $I_2$  intermediate is also subject to minor but non-negligible non-native contact formation of  $11.9(\pm 7.0)\%$ , while this is minimized in the  $I_1$  state at  $3.9(\pm 1.4)\%$ . In addition, the formation of  $40.3(\pm 8.7)\%$  of tertiary contacts in  $I_2$  signifies contact of Loop 2 within the minor groove of Stem 1 and initial structuring of this loop, which increases to  $53.7(\pm 4.3)\%$  in the  $I_1$  intermediate, thus confirming that additional triple-helix structure is present in the more native  $I_1$  state. Comparing overall size and native character, the  $I_1$  and  $I_2$  intermediates are quite similar, as demonstrated in Figure 4 and Table 1, and we posit that these two intermediates are non-differentiable via many experimental probes. Taken together,  $I_1$  and  $I_2$  are consistent with both the statistical mechanical model of Chen and coworkers that predicted a similar intermediate for BWYV (which shares similar sequence and structure with PLRV) (31) and the simulation-based results of Cho *et al.* for cases in which one stem is thermodynamically more stable than the other (30).

*Unfolded States.* Also labeled in Figure 4c are the three unfolded states observed in our simulations, denoted numerically as  $U_1$  through  $U_3$  (from most to least structured), which were identified as having little-to-no native structure and exhibiting a relatively low quantity of non-native structure (less than approximately one third of the maximum observed NNC). While Bian *et al.*, who recently reported 3  $\mu$ s of bias-exchange metadynamics simulations of a similar H-type pseudoknot, did not report discrete sub-states within their sampling of the unfolded state, our results are in agreement with their observation of multiple clusters of unfolded conformations at various  $R_g$  values (32).

The simplest of our observed unfolded states, the relatively extended  $U_3$  state, which has a mean gyration radius of  $\sim 22$  Å and a mean RMSD of  $\sim 20$  Å, exhibits only  $0.05(\pm 0.07)\%$  native character and a mean non-native contact quantity of  $22.5(\pm 11.8)\%$ , with these NNC's forming between apparently random segments of the PLRV sequence. The more structured  $U_1$  state represents the collapsed, or globular, portion of the unfolded conformational space, with a near-native mean gyration radius of  $\sim 13$  Å and a mean RMSD of  $\sim 12$  Å, and exhibits  $16.7(\pm 2.7)\%$  of native contacts, including mean Stem 1 and Stem 2 native contact counts of  $34.3(\pm 8.2)\%$  and  $11.9(\pm 19.5)\%$ , respectively, thereby indicating that stem nucleation may occur within this region of the conformational space, as might the reversing of such nucleation, *sans* the formation of loop or tertiary contacts. As the mean quantity of non-native contacts for  $U_1$  was  $32.7(\pm 15.2)\%$

(Table 1), it could be argued that this is a misfolded rather than unfolded state. Our classification of  $U_1$  as an unfolded state is based primarily upon the presence of this state along the folding pathway, in which it readily transitions to and from the less-native  $U_2$  state and the  $I_3$  intermediate described above, as well as the observation that nearly half of the detected non-native contacts within this state occur between the first three residues (5' terminus) and the 5 residues directly succeeding them, indicating dominance of highly-accessible local interactions rather than long-range or large scale structure formation.

Between these extremes, the  $U_2$  state is composed of moderately-collapsed, self-interacting conformations with an average RMSD of nearly 16 Å and a mean gyration radius of approximately 17 Å. The 7.2(±1.9)% mean native contact percentage accounts for the 18.0(±5.2)% mean Stem 1 native contacts that are observed in this state, again suggesting nucleation of Stem 1 early in the folding process, with no other native structure observed. As with  $U_1$ , non-native content is seemingly high for an unfolded state at 34.0(±9.2)%. As with both  $U_1$  and  $U_3$ , however, the  $U_2$  state is categorized as unfolded rather than misfolded based on the random occurrence of low-probability non-native contacts across the PLRV sequence and the observation that this state readily transitions to and from both the  $U_1$  and  $U_3$  portions of the configurational space.

*Misfolded States.* Three misfolded states are observed in Figure 4c, labeled  $M_1$  through  $M_3$ , where designation as a misfold was based on high RMSD (> 5 Å), low native state structural content (NC), and high degrees of non-native structure (NNC), as is consistent with a recent study of Noe and coworkers (33). While RNA is known to be easily trapped in metastable misfolded structures (34) and misfolding has been predicted or observed for this and numerous other pseudoknots (35-38), we emphasize that our normalization of the total number of non-native contacts present in a structure (using the largest total quantity of NNC observed) may underscore the overall degree of misfolding present for a given structural state.

The most native-like misfold,  $M_1$ , includes a native-like mean gyration radius of 12.3(±0.8) Å, a mean RMSD of only 8.0(±0.7) Å, and 21.7(±3.9)% of native structure formed. This latter value derives predominantly from the partial formation of Loop 1 (~67%), Stem 1 (~42%), and Stem 2 (~13% NC), suggesting that this misfolded state can include nucleation of either, or both, helical stem regions. The  $M_1$  non-native structural content of 37.4(±13.5)%

derives from interactions involving Loop 2 residues: in this case, more specifically, residues 21 – 25 may fold back to interact with either strand within Stem 1 (the 5' terminus or residues 15 – 17).

While the  $M_2$  state also exhibits a native-like gyration radius of  $12.3(\pm 0.4)$  Å, the mean RMSD of  $\sim 11$  Å and the limited native structure ( $\sim 10\%$ ), in tandem with a much higher mean non-native structure,  $65.5(\pm 7.9)\%$ , makes it clear that this misfold is only native-like in size. The small quantity of native structure observed in this state includes only the possible nucleation of Stem 1 ( $\sim 15\%$  of Stem 1 NC) and minimal, random formation of native tertiary interactions ( $\sim 12\%$  of native tertiary NC). The large quantity of non-native structure present in the  $M_2$  state includes mispairing of the 5' terminal G3 residue with A8 or C10, or with nucleotides 22 – 25, as well as possible mid-sequence mispairing of residues 7 – 14 with residues 11 – 22, the latter of which would maintain significant entropy in one or more loop regions. In addition, it might be speculated that the  $M_1$  and  $M_2$  misfolds would not be easily differentiable experimentally, given their similar size and lack of native structure.

Unlike the  $M_1$  and  $M_2$  misfolds, the  $M_3$  state exhibits a slightly larger mean gyration radius of  $14.5(\pm 1.9)$  Å and a somewhat higher mean RMSD of  $13.8(\pm 1.6)$  Å. Although collapsed to nearly native-like size, no native structure is observed in this state and the mean quantity of non-native contacts is observed to be  $46.1(\pm 16.8)\%$ , which is based largely on interactions between C14/G15/C16 Stem 1 residues with either the 5' terminus or with C10/G11 Stem 2 residues. While the  $M_1$  through  $M_3$  misfolds might easily be clustered or classified into a larger number of misfolded states, our analysis has emphasized macroscopically measurable structural characteristics and both  $M_2$  and  $M_3$  represent misfolds predicted by the statistical mechanical model of Ansari and coworkers (29).

**Macrostate Folding Mechanism**

Per the discussion above, Figure 6 presents the conformational dynamics observed within our ensemble simulations, with residues in each structure color coded according to their participation in native state secondary structure following the scheme used in Figure 5. Relative timescales in Figure 6 are indicated by colored arrows representing the nanosecond (green) through microsecond (red) regimes. The observed transition timescales are in agreement with well-characterized timescales reviewed by Isambert (39) and more recently reported by Truex *et al.*

(40), with zipping/unzipping transitions occurring on timescales of 100 ns or less and formation of helix stem regions on longer timescales (41,42), all much more rapid than accepted RNA transcription rates of approximately 50 nt/s, which suggests that folding and misfolding can easily occur during this process given the right environmental conditions.

As depicted in Figure 6, multiple folding pathways may be realized through the multiple intermediate and misfolded states described above. While the observed macrostates are generally distinguishable based on their native and non-native character (Table 1), nearly all exhibit highly-collapsed mean molecular size, with native or near-native gyration radii, thereby emphasizing the prevalence of self-interaction and collapse in initiating non-bonded interactions and folding of the pseudoknot motif, as was reported in the recent computational study of Bian *et al.* (32). The relative organization of native secondary structural elements and tertiary structure can be inferred from the free energy projections in Figure 7. Specifically, the formation of Stem 1 preceding that of Stem 2 is a prevalent occurrence in our simulations (Figure 7a), as predicted by the statistical mechanical model of Chen *et al.* (31) and the stability hypothesis put forth by Thirumalai and coworkers (30), the latter of which dictates that base-paired stem regions with higher thermodynamic stability will form before less-stable stem regions.

It is questionable, however, whether our observed prevalence of early Stem 1 formation is kinetically favored based not on relative stem thermodynamic stabilities, but rather on the sequence distance separating the strands within each stem. For example, Figure 1a shows that only 6 nt separate the terminal base-pair residues of Stem 1 in PLRV, whereas 14 nt separate the terminal base-pair of Stem 2, and it is therefore not surprising that a random search of the conformational space would favor Stem 1 nucleation over that of Stem 2. Notably, the use of stem-strand-sequence-separation as a predictor of the order of stem formation accurately accounts for the folding mechanisms of the MMTV, SRV-1, and hTR pseudoknots studied by Thirumalai and coworkers (30).

As would be expected, given that the formation of native tertiary structure involves interactions of Loop 2 residues with the minor groove of Stem 1, significant tertiary structure is absent until 50% or more of Stem 1, the stem with the much smaller stem-strand-sequence-separation, is formed (Figure 7b). A strong correlation between the formation of Loop 2 and tertiary contacts is evident in Figure 7c at low to moderate native contact values, with somewhat larger quantities of tertiary contacts and somewhat fewer Loop 2 contacts seemingly favored,

suggesting that the formation of tertiary structure prompts further formation of Loop 2 structure. In contrast, at high native contact values the existence of alternative states that favor either increased Loop 2 structure or increased tertiary structure, but not both, reinforces our prior description of the transition between the alternative  $F_1$  and  $F_2$  native states. Given the quantitative descriptions of the observed intermediates above, alongside our sampling of the free energy landscape shown in Figure 7d, it can be inferred that Stem 2 largely forms prior to both Loop 2 and tertiary contact formation, but may also form later in the folding process, in tandem with the initiation of Loop 2 and tertiary contacts.

The folding mechanics reported herein are consistent with the unfolding of BWYV described by recent optical tweezer experiments and steered molecular dynamics simulations (43), and add a new level of complexity by accounting for the formation of non-native structure. The presence of multiple misfolded states on the free energy surface is in agreement with the PK5 pseudoknot pathway reported by Cao *et al.* (44), as well as the broadly applicable Kinetic Partitioning Mechanism (KPM) put forth by Thirumalai and coworkers, in which a population of unfolded molecules is assumed to split into two distinct groups that fold on different time scales defined by the presence of multiple intermediates and misfolds (45-47). From Figure 6, our ensemble simulations predict individual molecular folding events occurring on the hundreds-of-nanoseconds (along the most rapid pathway) to the multiple-microseconds timescales.

**Structure-Based Frameshifting**

As a highly efficient PRF-stimulating pseudoknot (9,14), this system exhibits structural features *in silico* that have been previously correlated with frameshifting efficacy. In both of the observed native states, stable base-triplet interactions between Loop 2 residues and the Stem 1 minor groove are observed, which have been shown to be a requirement for high-efficiency -1 PRF (48-50). These interactions, as well as the looped-out A19 residue that is available for potential interactions with the ribosome, are illustrated in Figure 5.

Previous studies used these structural features as evidence of frameshifting stimulation being favored by high-stability, rigid mRNA pseudoknots that would resist the mechanical unfolding that takes place at the ribosome (9). This supposition, however, has been contradicted by the work of Brierley and coworkers, who demonstrated a lack of correlation between -1 PRF and ribosomal pausing (51), and the work of Woodside and coworkers that illustrated that -1

PRF is not dependent on resistance to mechanical unfolding (8). Rather than mechanical blockage of the ribosome, it is now believed that the ribosome itself may act as a helicase, able to disrupt secondary structure during transcription (52,53).

More recent work has shown that high  $-1$  PRF efficiency is instead correlated with pseudoknot conformational plasticity (8), and our observed conformational dynamics is well in line with this observation: our simulations provide structural evidence for numerous partially folded intermediates and misfolded states that would be accessible upon refolding of the pseudoknot motif following mechanical unfolding at the ribosome. Moreover, our characterization of alternative native states and certain highly flexible residues in PLRV (Loop 1, Loop 2, and the U12 linker) indicates that this pseudoknot possesses great plasticity, both in terms of the number of available macrostates and significant flexibility within those macrostates, thus supporting the conformational plasticity-based model of  $-1$  programmed ribosomal frameshifting.

## CONCLUSION

Our rigorous sampling provides a detailed picture of pseudoknot conformational equilibrium and dynamics, and allows us to characterize PLRV as a flexible structure with significant fluctuations within, and between, numerous macrostates participating in this conformational equilibrium. We report herein the presence of two alternate native state conformations, in which a global topological twisting mode allows for alternation between optimizing Loop 2 contacts and tertiary contacts between that loop and the minor groove of the neighboring base-paired stem region. Three folding intermediates have been identified and characterized, as have multiple misfolded states. While misfolding has been the focus of many protein-oriented studies, less attention has been given to this topic with respect to nucleic acids, and we present here the first all-atom, simulation-based study of this nature to probe RNA misfolding.

Although our results are well-aligned with the stability hypothesis of Thirumalai and coworkers, which emphasizes the importance of helical stem stability in determining the order of stem formation, we offer an alternative quantity upon which stem formation order may be determined, which is consistent with the system studied herein and the systems studied previously by Thirumalai and coworkers. Namely, from geometric and statistical considerations, we propose that stem folding order may be predicted by the relative sequence distances between

adjacent strands that must find one another to form properly base-paired native stem regions (*i.e.* the stem-strand-sequence-separation).

While this effort represents a significant increase in the size of the RNA systems to which we have applied our all-atom computational approach (21,54-56), much is left to be probed with regard to pseudoknot folding and (mal)function, particularly when considering the effects of sequence mutations, deletions, and insertions. We look forward to expanding on these findings: indeed, the diversity of this data set is testament to the level of detail now achievable through MD simulation methods, which we expect will only continue to open new avenues of RNA investigation.

ACKNOWLEDGEMENTS

The authors would like to recognize the Folding@Home volunteers worldwide who contributed invaluable processor time to this effort; Dennis Chen and members of the Sorin laboratory for their valuable feedback and contributions; and Mitchell Miller for his helpful discussions.

FUNDING

AR acknowledges the MARC U\*STAR program, funded by NIH/NIGMS #T34GM008074. KN and ES acknowledge research support from the CNSM and CSULB. YG and DR thank Women & Philanthropy for providing undergraduate research scholarships to support their efforts.

REFERENCES

1. Rietveld, K., Van Poelgeest, R., Pleij, C.W.A., Van Boom, J.H. and Bosch, L. (1982) The tRNA-Uke structure at the 3' terminus of turnip yellow mosaic virus RNA. Differences and similarities with canonical tRNA. *Nucleic Acids Res.*, **10**, 1929-1946.

2. Florentz, C., Briand, J.P., Romby, P., Hirth, L., Ebel, J.P. and Glegé, R. (1982) The tRNA-like structure of turnip yellow mosaic virus RNA: structural organization of the last 159 nucleotides from the 3' OH terminus. *The EMBO Journal*, **1**, 269-276.

3. Joshi, S., Chapeville, F. and Haenni, A.L. (1982) Turnip yellow mosaic virus RNA is aminoacylated in vivo in Chinese cabbage leaves. *The EMBO Journal*, **1**, 935-938.



4. Sorin, E.J., Nakatani, B.J., Rhee, Y.M., Jayachandran, G., Vishal, V. and Pande, V.S. (2004) Does native state topology determine the RNA folding mechanism? *J. Mol. Biol.*, **337**, 789-797.
5. Giedroc, D.P., Theimer, C.A. and Nixon, P.L. (2000) Structure, stability and function of RNA pseudoknots involved in stimulating ribosomal frameshifting. *J. Mol. Biol.*, **298**, 167-185.
6. Giedroc, D.P. and Cornish, P.V. (2009) Frameshifting RNA pseudoknots: structure and mechanism. *Virus Res.*, **139**, 193-208.
7. Plant, E.P. (2012) In Garcia, M. (ed.), *Viral Genomes - Molecular Structure, Diversity, Gene Expression Mechanisms and Host-Virus Interactions*. InTech, pp. 91-122.
8. Ritchie, D.B., Foster, D.A. and Woodside, M.T. (2012) Programmed -1 frameshifting efficiency correlates with RNA pseudoknot conformational plasticity, not resistance to mechanical unfolding. *Proc. Natl. Acad. Sci. USA*, **109**, 16167-16172.
9. Pallan, P.S., Marshall, W.S., Harp, J., Jewett, F.C., 3rd, Wawrzak, Z., Brown, B.A., 2nd, Rich, A. and Egli, M. (2005) Crystal structure of a luteoviral RNA pseudoknot and model for a minimal ribosomal frameshifting motif. *Biochemistry*, **44**, 11315-11322.
10. Sponer, J., Sponer, J.E., Petrov, A.I. and Leontis, N.B. (2010) Quantum chemical studies of nucleic acids: can we construct a bridge to the RNA structural biology and bioinformatics communities? *J. Phys. Chem. B*, **114**, 15723-15741.
11. Herschlag, D., Allred, B.E. and Gowrishankar, S. (2015) From static to dynamic: the need for structural ensembles and a predictive model of RNA folding and function. *Curr. Opin. Struct. Biol.*, **30**, 125-133.
12. Wan, Y., Suh, H., Russell, R. and Herschlag, D. (2010) Multiple unfolding events during native folding of the Tetrahymena group I ribozyme. *J. Mol. Biol.*, **400**, 1067-1077.
13. Colussi, T.M., Costantino, D.A., Hammond, J.A., Ruehle, G.M., Nix, J.C. and Kieft, J.S. (2014) The structural basis of transfer RNA mimicry and conformational plasticity by a viral RNA. *Nature*, **511**, 366-369.
14. Kim, Y.-G., Maas, S., Wang, S.C. and Rich, A. (2000) Mutational study reveals that tertiary interactions are conserved in ribosomal frameshifting pseudoknots of two luteoviruses. *RNA*, **6**, 1157-1165.

15. Cornell, W.D., Cieplak, P., Bayly, C.I., Gould, I.R., Merz, K.M., Ferguson, D.M., Spellmeyer, D.C., Fox, T., Caldwell, J.W. and Kollman, P.A. (1995) A second generation force field for the simulation of proteins, nucleic acids, and organic molecules. *J. Am. Chem. Soc.*, **117**, 5179-5197.
16. Lindahl, E., Hess, B. and van der Spoel, D. (2001) GROMACS 3.0: a package for molecular simulation and trajectory analysis. *Molecular modeling annual*, **7**, 306-317.
17. Gluick, T.C., Wills, N.M., Gesteland, R.F. and Draper, D.E. (1997) Folding of an mRNA pseudoknot required for stop codon readthrough: effects of mono- and divalent ions on stability. *Biochemistry*, **36**, 16173-16186.
18. Jorgensen, W.L., Chandrasekhar, J., Madura, J.D., Impey, R.W. and Klein, M.L. (1983) Comparison of simple potential functions for simulating liquid water. *The Journal of Chemical Physics*, **79**, 926.
19. Berendsen, H.J.C., Postma, J.P.M., Van Gunsteren, W.F., Dinola, A. and Haak, J. (1984) Molecular-dynamics with coupling to an external bath. *J. Chem. Phys.*, **81**, 3684-3690.
20. Hess, B., Bekker, H., Berendsen, H.J.C. and Fraaije, J.G.E.M. (1997) LINCS: A linear constraint solver for molecular simulations. *J. Comput. Chem.*, **18**, 1463-1472.
21. Sorin, E.J. and Pande, V.S. (2005) Exploring the helix-coil transition via all-atom equilibrium ensemble simulations. *Biophys. J.*, **88**, 2472-2493.
22. Lu, X.-J. and Olson, W.K. (2003) 3DNA: a software package for the analysis, rebuilding and visualization of three-dimensional nucleic acid structures. *Nucleic Acids Res.*, **31**, 5108-5121.
23. Zagrovic, B., Sorin, E.J. and Pande, V. (2001)  $\beta$ -hairpin folding simulations in atomistic detail using an implicit solvent model. *J. Mol. Biol.*, **313**, 151-169.
24. Sorin, E.J., Rhee, Y.M. and Pande, V.S. (2005) Does water play a structural role in the folding of small nucleic acids? *Biophys. J.*, **88**, 2516-2524.
25. Mouro, Paulo R., de Godoi Contessoto, V., Chahine, J., Junio de Oliveira, R. and Pereira Leite, Vitor B. (2016) Quantifying Nonnative Interactions in the Protein-Folding Free-Energy Landscape. *Biophys. J.*, **111**, 287-293.
26. Nixon, P.L., Cornish, P.V., Suram, S.V. and Giedroc, D.P. (2002) Thermodynamic Analysis of Conserved Loop–Stem Interactions in P1–P2 Frameshifting RNA Pseudoknots from Plant Luteoviridae. *Biochemistry*, **41**, 10665-10674.

27. Yingling, Y.G. and Shapiro, B.A. (2006) The prediction of the wild-type telomerase RNA pseudoknot structure and the pivotal role of the bulge in its formation. *J. Mol. Graphics Model.*, **25**, 261-274.
28. Reiling, C., Khutsishvili, I., Huang, K. and Marky, L.A. (2015) Loop contributions to the folding thermodynamics of DNA straight hairpin loops and pseudoknots. *J. Phys. Chem. B*, **119**, 1939-1946.
29. Narayanan, R., Velmurugu, Y., Kuznetsov, S.V. and Ansari, A. (2011) Fast folding of RNA pseudoknots initiated by laser temperature-jump. *J. Am. Chem. Soc.*, **133**, 18767-18774.
30. Cho, S.S., Pincus, D.L. and Thirumalai, D. (2009) Assembly mechanisms of RNA pseudoknots are determined by the stabilities of constituent secondary structures. *Proc. Natl. Acad. Sci. USA*, **106**, 17349-17354.
31. Cao, S., Giedroc, D.P. and Chen, S.J. (2010) Predicting loop-helix tertiary structural contacts in RNA pseudoknots. *RNA*, **16**, 538-552.
32. Bian, Y., Zhang, J., Wang, J., Wang, J. and Wang, W. (2015) Free energy landscape and multiple folding pathways of an H-type RNA pseudoknot. *PLoS One*, **10**, e0129089.
33. Keller, B.G., Kobitski, A., Jaschke, A., Nienhaus, G.U. and Noe, F. (2014) Complex RNA folding kinetics revealed by single-molecule FRET and hidden Markov models. *J. Am. Chem. Soc.*, **136**, 4534-4543.
34. Thirumalai, D. and Woodson, S.A. (2000) Maximizing RNA folding rates: a balancing act. *RNA*, **6**, 790-794.
35. Kopeikin, Z. and Chen, S.-J. (2006) Folding thermodynamics of pseudoknotted chain conformations. *J. Chem. Phys.*, **124**, 154903.
36. Isambert, H. and Siggia, E.D. (2000) Modeling RNA folding paths with pseudoknots: application to hepatitis delta virus ribozyme. *Proc. Natl. Acad. Sci. USA*, **97**, 6515-6520.
37. Thirumalai, D., Lee, N., Woodson, S.A. and Klimov, D. (2001) Early events in RNA folding. *Annu. Rev. Phys. Chem.*, **52**, 751-762.
38. Chadalavada, D.M., Senchak, S.E. and Bevilacqua, P.C. (2002) The folding pathway of the genomic hepatitis delta virus ribozyme is dominated by slow folding of the pseudoknots. *J. Mol. Biol.*, **317**, 559-575.
39. Isambert, H. (2009) The jerky and knotty dynamics of RNA. *Methods*, **49**, 189-196.

- 1  
2  
3  
4  
5  
6  
7  
8  
9  
10  
11  
12  
13  
14  
15  
16  
17  
18  
19  
20  
21  
22  
23  
24  
25  
26  
27  
28  
29  
30  
31  
32  
33  
34  
35  
36  
37  
38  
39  
40  
41  
42  
43  
44  
45  
46  
47  
48  
49  
50  
51  
52  
53  
54  
55  
56  
57  
58  
59  
60
40. Truex, K., Chung, H.S., Louis, J.M. and Eaton, W.A. (2015) Testing Landscape Theory for Biomolecular Processes with Single Molecule Fluorescence Spectroscopy. *Phys. Rev. Lett.*, **115**, 018101.
41. Neupane, K., Ritchie, D.B., Yu, H., Foster, D.A., Wang, F. and Woodside, M.T. (2012) Transition path times for nucleic Acid folding determined from energy-landscape analysis of single-molecule trajectories. *Phys. Rev. Lett.*, **109**, 068102.
42. Neupane, K., Foster, D.A., Dee, D.R., Yu, H., Wang, F. and Woodside, M.T. (2016) Direct observation of transition paths during the folding of proteins and nucleic acids. *Science*, **352**, 239-242.
43. White, K.H., Orzechowski, M., Fourmy, D. and Visscher, K. (2011) Mechanical unfolding of the beet western yellow virus -1 frameshift signal. *J. Am. Chem. Soc.*, **133**, 9775-9782.
44. Cao, S. and Chen, S.J. (2007) Biphasic folding kinetics of RNA pseudoknots and telomerase RNA activity. *J. Mol. Biol.*, **367**, 909-924.
45. Thirumalai, D., Klimov, D.K. and Woodson, S.A. (1997) Kinetic partitioning mechanism as a unifying theme in the folding of biomolecules. *Theor. Chem. Acc.*, **96**, 14-22.
46. Lin, J.C., Hyeon, C. and Thirumalai, D. (2012) RNA under tension: Folding Landscapes, Kinetic partitioning Mechanism, and Molecular Tensegrity. *J Phys Chem Lett*, **3**, 3616-3625.
47. Chen, J., Gong, S., Wang, Y. and Zhang, W. (2014) Kinetic partitioning mechanism of HDV ribozyme folding. *J. Chem. Phys.*, **140**, 025102.
48. Liphardt, J., Naphthine, S., Kontos, H. and Brierley, I. (1999) Evidence for an RNA pseudoknot loop-helix interaction essential for efficient -1 ribosomal frameshifting. *J. Mol. Biol.*, **288**, 321-335.
49. Chen, G., Chang, K.Y., Chou, M.Y., Bustamante, C. and Tinoco, I., Jr. (2009) Triplex structures in an RNA pseudoknot enhance mechanical stability and increase efficiency of -1 ribosomal frameshifting. *Proc. Natl. Acad. Sci. USA*, **106**, 12706-12711.
50. Chou, M.Y. and Chang, K.Y. (2010) An intermolecular RNA triplex provides insight into structural determinants for the pseudoknot stimulator of -1 ribosomal frameshifting. *Nucleic Acids Res.*, **38**, 1676-1685.

- 1  
2  
3 51. Kontos, H., Naphthine, S. and Brierley, I. (2001) Ribosomal pausing at a frameshifter  
4 RNA pseudoknot is sensitive to reading phase but shows little correlation with frameshift  
5 efficiency. *Mol. Cell. Biol.*, **21**, 8657-8670.  
6  
7  
8  
9 52. Takyar, S., Hickerson, R.P. and Noller, H.F. (2005) mRNA Helicase Activity of the  
10 Ribosome. *Cell*, **120**, 49-58.  
11  
12 53. Qu, X., Wen, J.D., Lancaster, L., Noller, H.F., Bustamante, C. and Tinoco, I., Jr. (2011)  
13 The ribosome uses two active mechanisms to unwind messenger RNA during translation.  
14 *Nature*, **475**, 118-121.  
15  
16  
17 54. Sorin, E.J., Engelhardt, M.A., Herschlag, D. and Pande, V.S. (2002) RNA simulations:  
18 Probing hairpin unfolding and the dynamics of a GNRA tetraloop. *J. Mol. Biol.*, **317**,  
19 493-506.  
20  
21  
22 55. Sorin, E.J., Rhee, Y.M., Nakatani, B.J. and Pande, V.S. (2003) Insights into nucleic acid  
23 conformational dynamics from massively parallel stochastic simulations. *Biophys. J.*, **85**,  
24 790-803.  
25  
26  
27  
28 56. DePaul, A.J., Thompson, E.J., Patel, S.S., Haldeman, K. and Sorin, E.J. (2010)  
29 Equilibrium conformational dynamics in an RNA tetraloop from massively parallel  
30 molecular dynamics. *Nucleic Acids Res.*, **38**, 4856-4867.  
31  
32  
33  
34  
35  
36  
37  
38  
39  
40  
41  
42  
43  
44  
45  
46  
47  
48  
49  
50  
51  
52  
53  
54  
55  
56  
57  
58  
59  
60

Captions

**Figure 1.** *Luteovirus* pseudoknot: (a) sequence and secondary structure, with Stem 1 (S1) beginning at the 5' terminus, Stem 2 (S2) ending at the 3' terminus, and the locations of the C17U/A18C mutations noted by the dashed gray box; (b) three-dimensional representation of the crystal structure (PDB ID 2A43) with selected residues labeled to aid in visual orientation.

**Figure 2.** Simplified representation of our sampling technique along an idealized folding landscape. Each gray dot represents 200 independent simulations starting in a specific conformation at time  $t = 0$  in (a). After a short annealing period, these simulations rapidly sample from the entire free energy surface (b). At longer times, the ensemble relaxes into conformational equilibrium on this free energy surface and transitions between distinct structural states (examples provided by arrows) are observed (c).

**Figure 3.** Populations of the 27 conformational microstates identified by K-means clustering versus time (split into three panels for visual clarity). Approximate conformational equilibrium is established at 6.0 ns (dashed line).

**Figure 4.** Free energy surface projected onto the RMSD,  $R_g$ , and percentage of native and non-native contact folding metrics. State labels in (c) indicate observed macrostates participating in the equilibrium folding mechanism. Dashed lines are provided to visually align a given state depicted in neighboring projections. **The color-coded energy scale shown in (b) applies to all panels shown.**

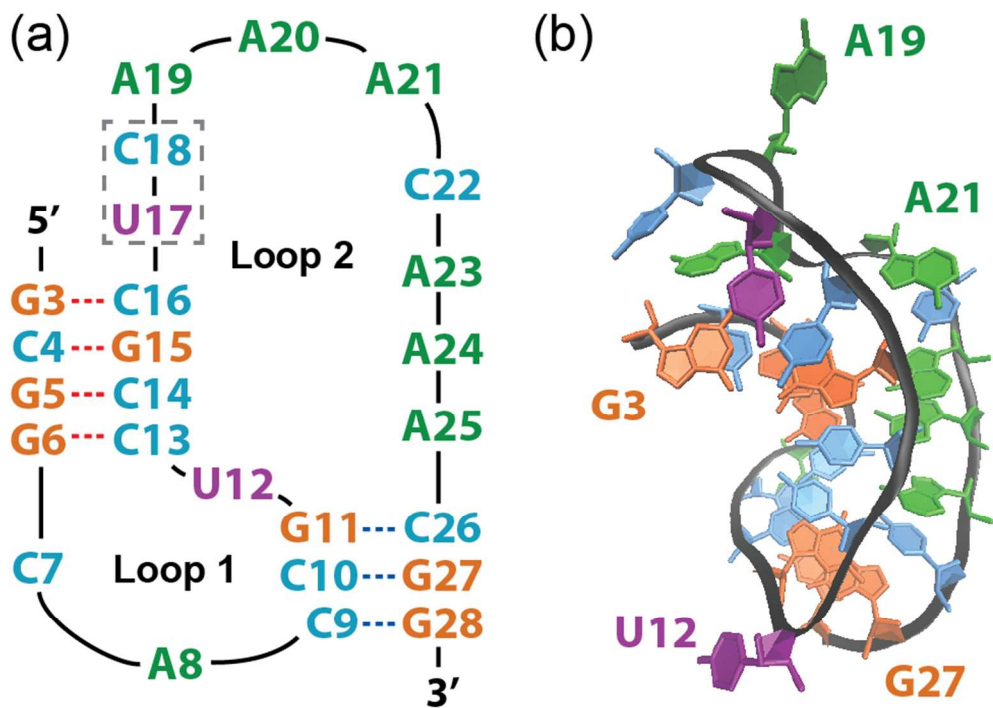
**Figure 5.** (a) The root-mean-squared fluctuation observed in our native state simulated ensemble, with residue labels denoting regions that show larger fluctuations than the baseline of approx. 2 Å. (b) Ensemble average structures of the PLRV pseudoknot native states,  $F_1$  (left) and  $F_2$  (right), with specific residues labeled and substructures colored for visual clarity, including Stem 1 (blue), Loop 1 (yellow), Stem 2 (red), and Loop 2 (green). (c) Native structures in (b) rotated 90° about the vertical axis for visual inspection. (d) Native structures shown in (a) and (b) oriented and presented to emphasize interactions of the relatively immobile A20 and A24 residues with Stem 1 base-pairs; hydrogen bonds are represented as dotted lines and transparent molecular surfaces are provided to visualize van der Waals contacts.

**Figure 6.** Pseudoknot macrostate folding mechanism predicted from our ensemble simulations following equilibration. Substructures are colored according to the color scheme used in Figure 5b and arrows are color-coded to represent transition timescales according to the inset key. For each macrostate the average structure is shown alongside the mean RMSD (top) and  $R_g$  (bottom).

**Figure 7.** Sampling of the PLRV pseudoknot conformational free energy landscape projected onto the native content of substructural elements S1, S2, L2, and T. **The color-coded energy scale shown in (b) applies to all panels shown.**

**Table 1.** Overall and substructure native and non-native contacts per macrostate

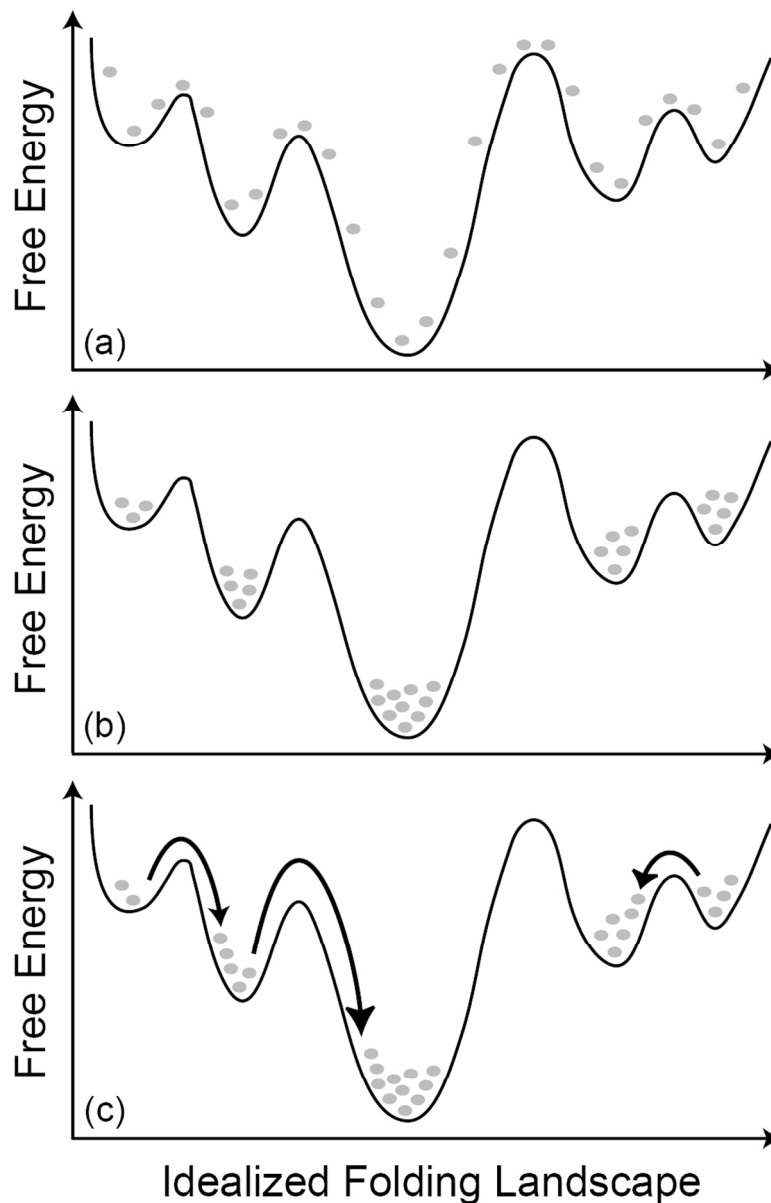
State	NC (%)	Non-NC (%)	S1 (%)	S2 (%)	L1 (%)	L2 (%)	T (%)
F <sub>1</sub>	97.2(5.6)	0.0(0.0)	97.6(6.8)	100.6(11.7)	99.7(42.1)	96.0(15.3)	68.7(7.3)
F <sub>2</sub>	95.7(4.0)	0.0(0.4)	98.2(8.1)	97.9(19.8)	96.9(35.6)	53.3(13.5)	79.4(10.5)
I <sub>1</sub>	67.8(3.9)	3.9(1.4)	97.4(6.9)	22.2(9.8)	92.1(47.4)	23.7(5.0)	53.7(4.3)
I <sub>2</sub>	50.5(6.2)	11.9(7.0)	73.9(18.7)	12.2(28.5)	21.3(43.7)	20.5(13.6)	40.3(8.7)
I <sub>3</sub>	33.7(3.3)	12.4(6.0)	84.7(11.4)	2.2(10.0)	0.7(5.9)	0.0(0.5)	0.9(2.0)
M <sub>1</sub>	21.7(3.9)	37.4(13.5)	41.7(9.1)	13.0(13.0)	66.8(59.0)	0.3(1.4)	6.5(4.8)
M <sub>2</sub>	9.8(2.0)	65.5(7.9)	14.6(3.9)	0.1(0.9)	0.5(7.0)	0.4(1.6)	9.8(3.8)
M <sub>3</sub>	0.7(0.8)	46.1(16.8)	0.6(1.5)	0.1(0.9)	0.6(6.6)	0.7(2.2)	0.8(1.2)
U <sub>1</sub>	16.7(2.7)	32.7(15.2)	34.3(8.2)	11.9(19.5)	1.6(11.3)	0.9(2.4)	2.8(3.8)
U <sub>2</sub>	7.2(1.9)	34.0(9.2)	18.0(5.2)	0.1(1.9)	0.2(3.8)	0.3(2.0)	0.3(1.1)
U <sub>3</sub>	0.5(0.7)	22.5(11.8)	0.2(0.9)	0.0(0.2)	0.3(5.2)	0.1(1.0)	1.0(1.6)



(Single Column) Figure 1. *Luteovirus* pseudoknot: (a) sequence and secondary structure, with stem 1 (S1) beginning at the 5' terminus, stem 2 (S2) ending at the 3' terminus, and the locations of the C17U/A18C mutations noted by the dashed gray box; (b) three-dimensional representation of the crystal structure (PDB ID 2A43) with selected residues labeled to aid in visual orientation.

83x59mm (300 x 300 DPI)

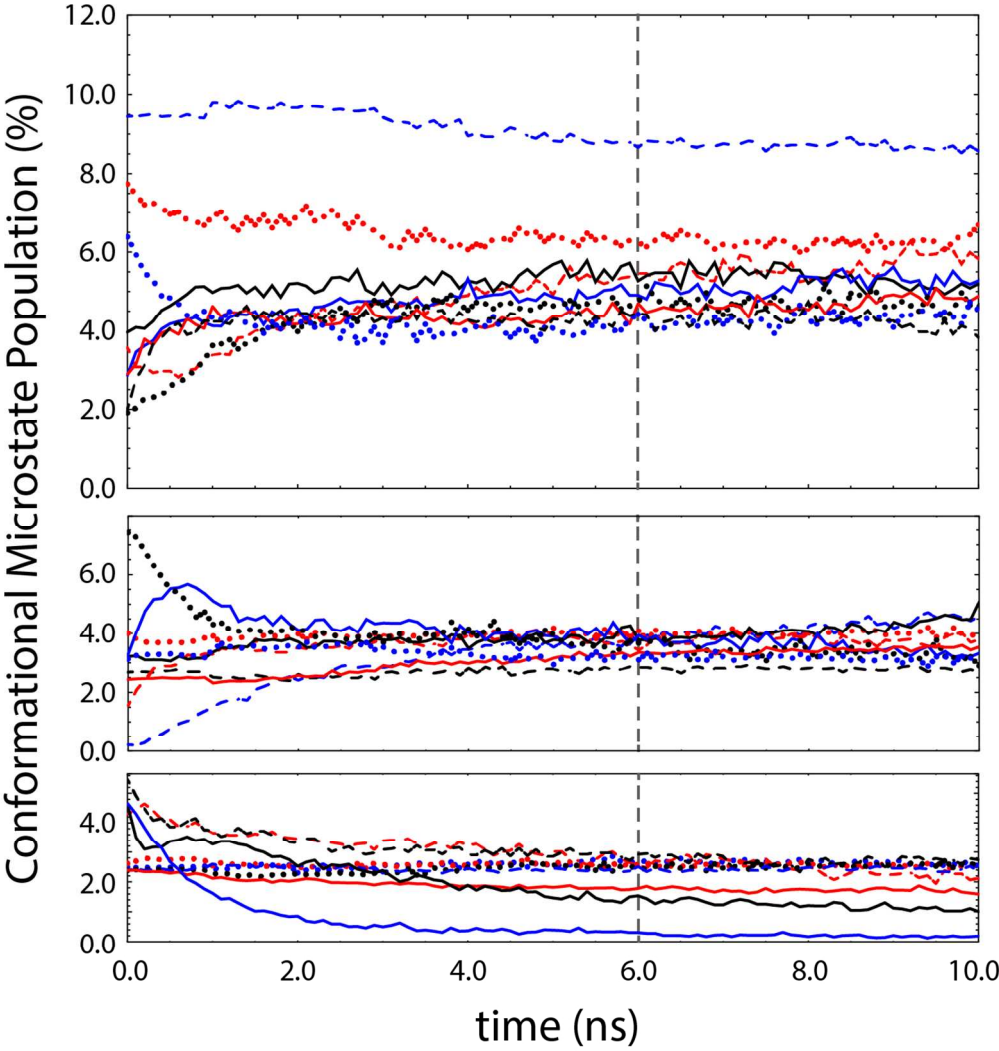




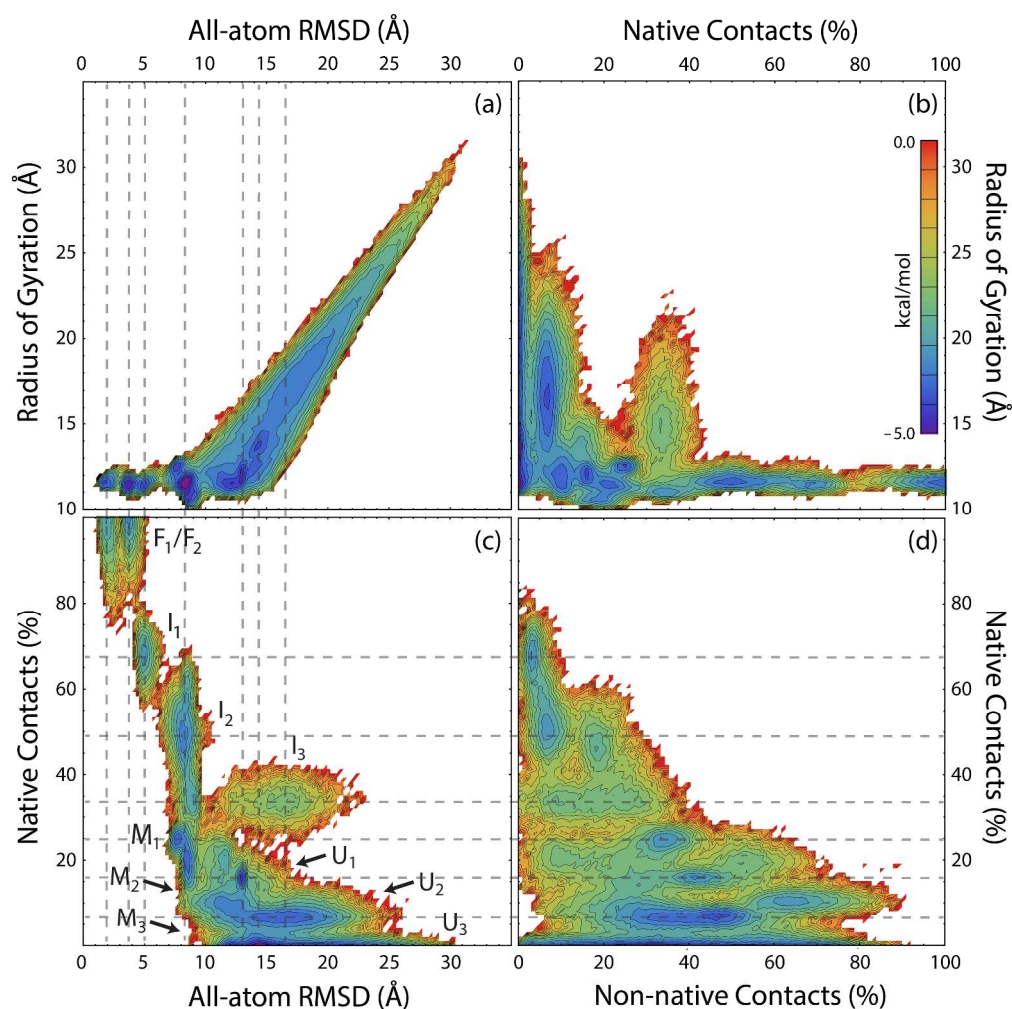
(Single Column) Figure 2. Simplified representation of our sampling technique along an idealized folding landscape. Each gray dot represents 200 independent simulations starting in a specific conformation at time  $t = 0$  in (a). After a short annealing period, these simulations rapidly sample from the entire free energy surface (b). At longer times, the ensemble relaxes into conformational equilibrium on this free energy surface and transitions between distinct structural states (examples provided by arrows) are observed (c).

Figure 2

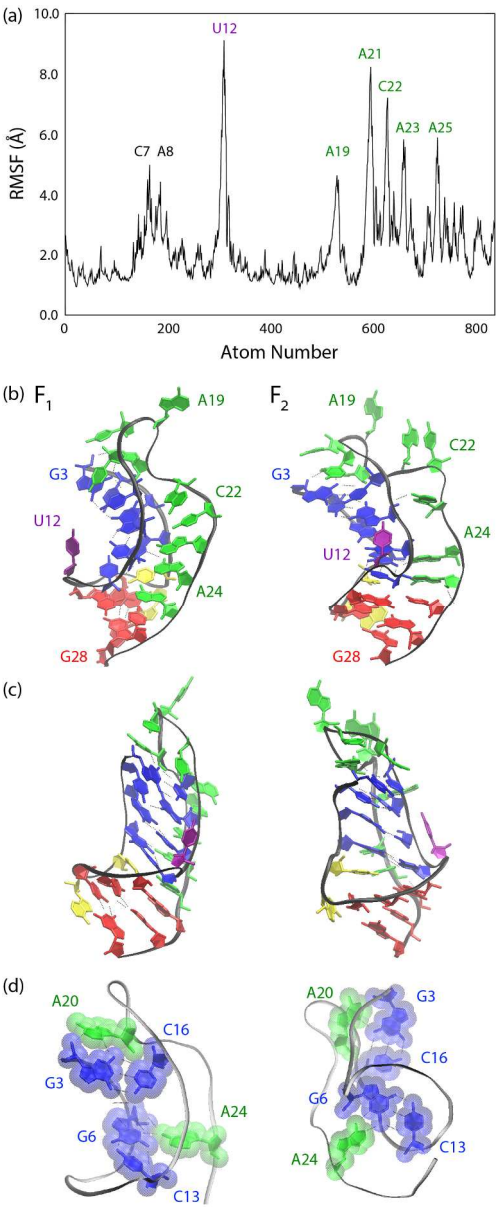
84x131mm (300 x 300 DPI)



(Single Column) Figure 3. Populations of the 27 conformational microstates identified by K-means clustering versus time (split into three panels for visual clarity). Approximate conformational equilibrium is established at 6.0 ns (dashed line).  
Figure 3  
122x128mm (300 x 300 DPI)

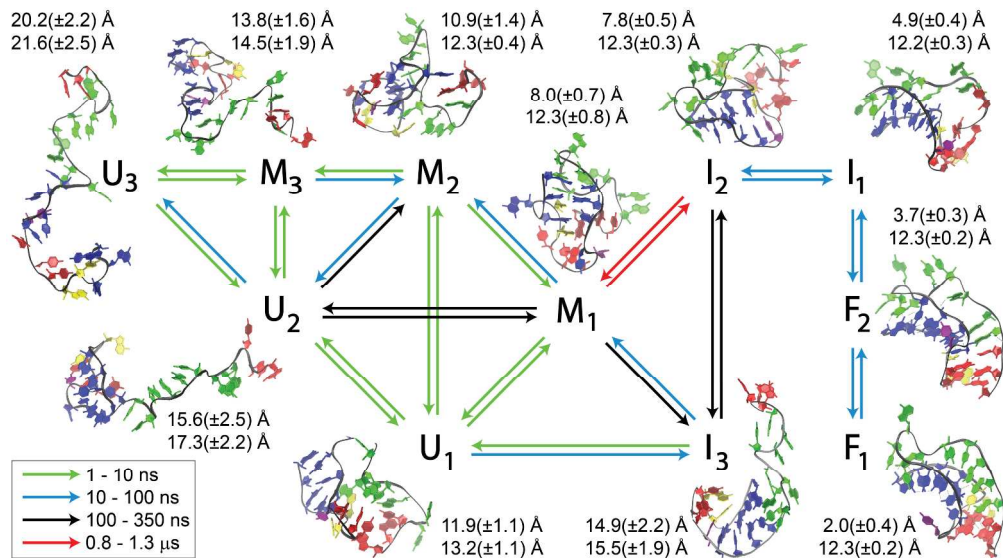


(Double Column) Figure 4. Free energy surface projected onto the RMSD,  $R_g$ , and percentage of native and non-native contact folding metrics. State labels in (c) indicate observed macrostates participating in the equilibrium folding mechanism. Dashed lines are provided to visually align a given state depicted in neighboring projections. The color-coded energy scale shown in (b) applies to all panels shown.



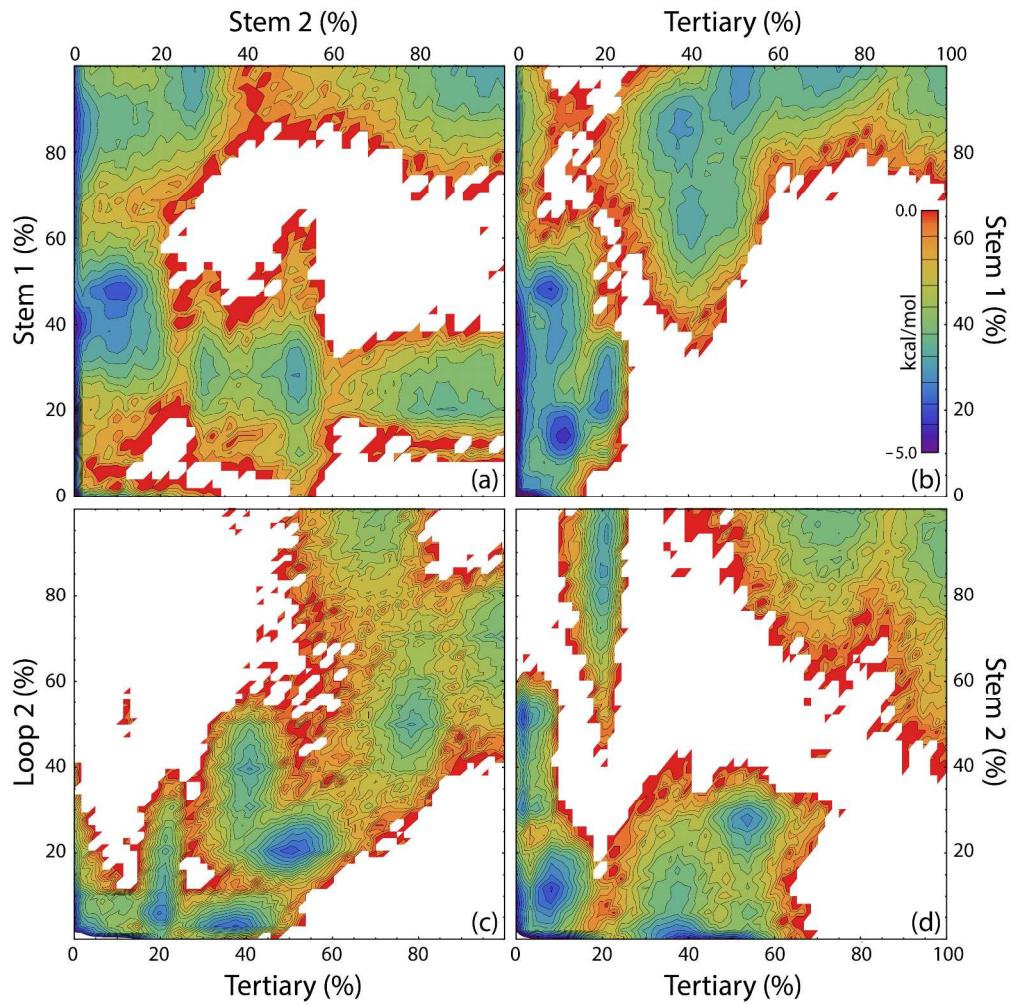
(Single Column) Figure 5. (a) The root-mean-squared fluctuation observed in our native state simulated ensemble, with residue labels denoting regions that show larger fluctuations than the baseline of approx. 2 Å. (b) Ensemble average structures of the PLRV pseudoknot native states, F<sub>1</sub> (left) and F<sub>2</sub> (right), with specific residues labeled and substructures colored for visual clarity, including Stem 1 (blue), Loop 1 (yellow), Stem 2 (red), and Loop 2 (green). (c) Native structures in (b) rotated 90° about the vertical axis for visual inspection. (d) Native structures shown in (a) and (b) oriented and presented to emphasize interactions of the relatively immobile A20 and A24 residues with Stem 1 base-pairs; hydrogen bonds are represented as dotted lines and transparent molecular surfaces are provided to visualize van der Waals contacts.

105x258mm (300 x 300 DPI)



(Double Column) Figure 6. Pseudoknot macrostate folding mechanism predicted from our ensemble simulations following equilibration. Substructures are colored according to the color scheme used in Figure 5b and arrows are color-coded to represent transition timescales according to the inset key. For each macrostate the average structure is shown alongside the mean RMSD (top) and Rg (bottom).





(Double Column) Figure 7. Sampling of the PLRV pseudoknot conformational free energy landscape projected onto the native content of substructural elements S1, S2, L2, and T. The color-coded energy scale shown in (b) applies to all panels shown.

299x302mm (300 x 300 DPI)